INTERNATIONAL JOURNAL FOR NUMERICAL METHODS IN BIOMEDICAL ENGINEERING
Int. J. Numer. Meth. Biomed. Engng. 2014; **30**:545–562
Published online 13 January 2014 in Wiley Online Library (wileyonlinelibrary.com). DOI: 10.1002/cnm.2618

A physically motivated constitutive model for 3D numerical simulation of skeletal muscles

J. Weickenmeier [1], M. Itskov [2], E. Mazza [1,3] and M. Jabareen [4,*,†]

[1] *Department of Mechanical and Process Engineering, ETH Zurich, Zurich, Switzerland*
[2] *Department of Continuum Mechanics, RWTH Aachen University, Aachen, Germany*
[3] *Swiss Federal Laboratories for Materials Science and Technology, EMPA Duebendorf, Duebendorf, Switzerland*
[4] *Faculty of Civil and Environmental Engineering, Technion – Israel Institute of Technology, Haifa, Israel*

SUMMARY

A detailed numerical implementation within the FEM is presented for a physically motivated three-dimensional constitutive model describing the passive and active mechanical behaviors of the skeletal muscle. The derivations for the Cauchy stress tensor and the consistent material tangent are provided. For nearly incompressible skeletal muscle tissue, the strain energy function may be represented either by a coupling or a decoupling of the distortional and volumetric material response. In the present paper, both functionally different formulations are introduced allowing for a direct comparison between the coupled and decoupled isochoric-volumetric approach. The numerical validation of both implementations revealed significant limitations for the decoupled approach. For an extensive characterization of the model response to different muscle contraction modes, a benchmark model is introduced. Finally, the proposed implementation is shown to provide a reliable tool for the analysis of complex and highly nonlinear problems through the example of the human mastication system by studying bite force and three-dimensional muscle shape changes during mastication. Copyright © 2014 John Wiley & Sons, Ltd.

Received 17 July 2013; Revised 26 September 2013; Accepted 8 November 2013

KEY WORDS: soft biological tissue; skeletal muscle; muscle activation; mastication system; numerical implementation; tangent modulus

1. INTRODUCTION

The skeletal muscle fulfills several different functions in the human body providing support to the skeletal system, enabling body movement, or any other voluntary active tissue response such as in facial expressions, speech, and mastication. Skeletal muscle in humans differs from other muscle tissue types such as smooth or cardiac muscle through its ability to be activated voluntarily by the somatic nervous system. Similarly to most soft biological tissues, a muscle may undergo large deformations and is characterized by a highly nonlinear deformation response. Its hierarchical structure, consisting of fascicles of myocytes or muscle cells on the macrolevel reaching down to the basic functional unit of muscle, that is, the sarcomere, spans across several length scales [1, 2].

Unlike most other soft tissues, the ability to actively contract allows the muscle to produce tensile force upon neural stimulation. Extensive mechanical characterization of muscle properties began with Hill's phenomenological three element model [3]. This formulation captures the fundamental relationship between contraction velocity and tensile force in the fully tetanized muscle observed in pioneering experiments on individual muscle fibers. However, the underlying contraction

*Correspondence to: M. Jabareen, Faculty of Civil and Environmental Engineering, Technion – Israel Institute of Technology, Haifa, Israel.

†E-mail: cvjmah@tx.technion.ac.il

mechanism was not understood until Huxley proposed the micromechanically based cross-bridge theory [4]. The Hill model provides a simple formulation of the active properties of the muscle on the tissue level and has been used and extended in many different model formulations [1, 5–7]. Most constitutive laws proposed in literature consider a one-dimensional (1D) formulation in order to describe the interaction between muscle, tendons, and joints within the musculoskeletal system [8–12]. However, appropriate modeling of the interaction between muscle and its surrounding tissue requires a 3D representation allowing for a physical prediction of transversal and volumetric material response. Several models describing the contractile properties on a continuum level have been proposed in recent years of which most make use of a phenomenological description of the underlying tissue behavior [13–21]. Moreover, constitutive models were proposed describing the electromechanical coupling in the skeletal muscle [22–24] and skeletal muscle fatigue [24–26]. Representation of the electromechanical coupling was applied to model active behavior of cardiac muscles [27–29]. Other work aims at describing phenomena such as stretch-induced muscle growth [30] and muscle damage [31].

In general, a 3D continuum approach provides the basis for an effective description of nonlinear, anisotropic material behavior including the possibility to represent different muscle fiber distributions and pennation angles. Alongside the advances in mathematical modeling of the muscle tissue, new experimental methods allow for more comprehensive validation procedures of the proposed constitutive formulations. These recent developments include improved experimental setups to characterize the passive properties of the muscle [32], visualization of muscle deformation behavior during contraction [33, 34], and the application of the elastography method to determine stiffness properties of the muscle [35, 36].

The development of mathematical muscle models provided substantial understanding of active tissue behavior in the human body. Examples are the simulation of muscle driven locomotion where rigid body systems together with 1D muscle formulations [9, 37, 38] are implemented in the finite element (FE) environment to improve our understanding of muscle response and its interaction with surrounding tissues [39–41]. Other examples are given by detailed FE simulations of the tongue [42], the human upper airway [43], or the forces during mastication [20].

Finite element simulations require the implementation of active or passive constitutive models. Hence, on the basis of constitutive equations governing the material response at a continuum level, the consistent linearization of the strain energy function, the stress tensor, and the associated material tangent must be provided for numerical calculation, which is missing in all previously mentioned publications. The muscle model considered here is based on the work of Böl and Reese (2008) [44], Ehret (2011) [45], and Ehret *et al.* (2011) [15]. Most constitutive material laws for muscle proposed so far make use of an additive split of muscle tissue stress into a passive and an active part. This approach is mainly due to experimental practice where the muscle responses are compared in the resting and activated states. However, this modeling approach ignores experimental evidence that the sarcomere system is not a purely active muscle component [15, 46, 47]. Ehret *et al.* (2011) [15] avoided this explicit additive split of muscle stress and presented a phenomenologically based material model that provides significant control of several different contractile characteristics of the skeletal muscle. This model assumes the muscle tissue as incompressible. Model implementation in a FE program using a material subroutine does not allow to enforce volume preservation. For this reason, a modified formulation is introduced here without incompressibility condition. We first present the implementation of the new set of equations in the FE environment. Next, the consistent linearization of the strain energy function, the Cauchy stress tensor $\boldsymbol{\sigma}$, and the associated spatial form of the material tangent c are derived. The implementation of the strain energy function was carried out for two functionally different formulations of the muscle model allowing for a direct comparison between the so-called coupled and decoupled approach. The decoupled approach refers to the additive split of the strain energy function into a volumetric and a purely isochoric part as proposed by Flory (1961) [48]. This widely used approach is compared to a formulation avoiding this decomposition. It is shown that the volumetric-isochoric split leads to negative eigenvalues of the spatial tangent modulus c and to an unphysical volume behavior for the activated muscle state. This unphysical volumetric response has already been observed for different material models of passive, fiber-reinforced soft tissues by Helfenstein *et al.* (2010) [49].

DOI: 10.1002/cnm

Finally, our FE implementation is applied in a realistic simulation of bite force resulting from the contraction of the masseter muscle. This example is used to demonstrate the predictive capabilities of the model implementation with respect to shape changes of geometrically complex muscles and the development of bite force during mastication.

2. FINITE ELEMENT IMPLEMENTATION

On the basis of a muscle model presented in Ehret *et al.* (2011) [15, 45], a constitutive model formulation is proposed for the passive and active behavior of skeletal muscles. The formulation makes use of the generalized invariants representation including a term that controls the muscle activation. While the constitutive model proposed by Ehret *et al.* (2011) considers muscle as a fully incompressible tissue, there is no experimental evidence found in literature that would indicate such behavior. Moreover, the numerical implementation of a fully incompressible material within the FE environment entails significant challenges in providing adequate approximation schemes and cannot be realized using a material subroutine. Hence, muscle tissue is considered here as a nearly incompressible material, thus, allowing for an adequate physical approximation of the mechanical response. For comparison reasons, two different functional forms for the constitutive formulation of the muscle tissue with and without the additive volumetric-isochoric split of the strain energy function are introduced. To the best of our knowledge, the derivations of the stress tensor and the consistent material tangent for both approaches are presented here for the first time.

2.1. Active skeletal muscle model

The first functional form of the strain energy function presented here is given as a function of the right Cauchy Green tensor $\mathbf{C} = \mathbf{F}^T\mathbf{F}$ as

$$W = \frac{1}{4}\mu\left\{\frac{1}{\alpha}\left(\exp\left[\alpha\left(\tilde{I}-1\right)\right]-1\right)+\frac{1}{\beta}\left(\exp\left[\beta\left(\tilde{J}-1\right)\right]-1\right)+\frac{1}{\gamma}\left(III_C^{-\gamma}-1\right)\right\},$$
$$\tilde{I} = \mathbf{C}\colon\left(\tilde{\mathbf{L}}+w_a\mathbf{M}\right),\quad \tilde{J} = \operatorname{cof}(\mathbf{C})\colon\tilde{\mathbf{L}},\quad III_C = \det(\mathbf{C}), \tag{1}$$

where μ, α, β, and γ are material parameters. $\tilde{I}$, $\tilde{J}$, and III_C are three invariants of $\mathbf{C}$ expressed in terms of the structural tensor $\tilde{\mathbf{L}}$ given by

$$\tilde{\mathbf{L}} = \frac{w_0}{3}\mathbf{I} + w_p\mathbf{M}. \tag{2}$$

Material anisotropy is governed by the structural tensor $\mathbf{M} = \mathbf{m}\otimes\mathbf{m}$, where $\mathbf{m}$ is the unit vector parallel to the preferred muscle fiber direction in the reference configuration. The identity tensor of second order $\mathbf{I}$ serves to describe the passive isotropic properties of muscles. The weighing parameters w_0 and w_p govern the ratio between muscle matrix material (w_0) and muscle fibers (w_p), with $w_0 + w_p = 1$. In this formulation, an activation parameter w_a is introduced, which affects the generalized invariant $\tilde{I}$. The magnitude of w_a is correlated to the current level of the muscle activation and is governed by a physically based activation function described in the succeeding texts.

The second functional form that makes use of the volumetric-isochoric split of the strain energy function is given by

$$\bar{W} = \bar{W}_{iso}\left(\bar{\mathbf{C}}\right)+\bar{W}_{vol}(J),$$
$$\bar{W}_{iso}\left(\bar{\mathbf{C}}\right) = \frac{\mu}{4}\left\{\frac{1}{\alpha}(\exp\left[\alpha\left(\bar{\tilde{I}}-1\right)\right]-1)+\frac{1}{\beta}(\exp\left[\beta\left(\bar{\tilde{K}}-1\right)\right]-1)\right\},$$
$$\bar{W}_{vol}(J) = \frac{\kappa}{4}[J^2-1-2\ln(J)], \tag{3}$$

where μ, α, β, and κ are material parameters and

$$\bar{\tilde{I}} = \bar{\mathbf{C}}\colon\left(\tilde{\mathbf{L}}+w_a\mathbf{M}\right),\quad \bar{\tilde{K}} = \bar{\mathbf{C}}^{-1}\colon\tilde{\mathbf{L}},\quad J = \det\mathbf{F}. \tag{4}$$

DOI: 10.1002/cnm

In this formulation, $\bar{\mathbf{C}}$ represents the unimodular right Cauchy–Green tensor that renders a pure measure of distortion and is defined by

$$\bar{\mathbf{C}} = J^{-2/3}\mathbf{C}. \tag{5}$$

The choice of the volumetric part $\bar{W}_{vol}$ in (3) is based on the strong polyconvexity condition and sufficient growth for large strains in order to penalize considerable volume changes. Substantial work on this topic has been carried out by Neff *et al.* (2003) [50, 51].

Both formulations presented in Equations (1–5) represent new constitutive models describing the active tissue response. It can be shown that these two formulations coincide only for the case of ideal incompressibility. In this special case, these strain energy functions correspond to the ones presented by Ehret *et al.* (2011) [15].

In the following, the strain energy function W (1) will be referred to as the *coupled formulation* and the strain energy function $\bar{W}$ (3) as the *decoupled formulation*. Relevant components of the active elements in both model formulations are presented here on the basis of the corresponding equations in [15, 44]. This set of equations constitutes the basis for the derivation of the stress tensor and the consistent material tangent. As mentioned in the previous texts, the activation level of the muscle is governed by the parameter w_a determined by [15]

$$w_a = \begin{cases} 0 & \text{if } P_{act} = 0, \\ \frac{W_0(\chi^\star)}{\alpha\lambda_m^2} - \frac{\tilde{I}_p'}{2\lambda_m} & \text{else,} \end{cases} \tag{6}$$

where $W_0(\chi^\star)$ denotes the solution for the principal branch of the Lambert-W function, and $\chi^\star$ is given by [15, 52]

$$\chi^\star = P_{act}\frac{2\alpha\lambda_m}{\mu}\exp\left[\left(\frac{\alpha}{2}\right)\left(2 - 2\tilde{I}_p + \lambda_m\tilde{I}_p'\right)\right] + \frac{\alpha}{2}\lambda_m\tilde{I}_p'\exp\left[\left(\frac{\alpha}{2}\right)\lambda_m\tilde{I}_p'\right]. \tag{7}$$

Here, the squared fiber stretch λ_m, the passive part of the first generalized invariant $\tilde{I}_p$, and its first derivative with respect to fiber stretch λ_m, $\tilde{I}_p'$, are defined by [15]

$$\lambda_m = \sqrt{\mathbf{C}:\mathbf{M}}, \tag{8}$$

$$\tilde{I}_p = \frac{w_0}{3}\left(\lambda_m^2 + \frac{2}{\lambda_m}\right) + w_p\lambda_m^2, \tag{9}$$

$$\tilde{I}_p' = \frac{\partial\tilde{I}_p}{\partial\lambda_m} = \frac{w_0}{3}\left(2\lambda_m - \frac{2}{\lambda_m^2}\right) + 2w_p\lambda_m. \tag{10}$$

The nominal stress P_{act} due to the activation of the muscle is expressed in terms of an activation function as [15, 44]

$$P_{act} = f_\zeta f_v\, Na \sum_{i=1}^{n_{\mathrm{MU}}}\rho_i F_t^i, \tag{11}$$

where $Na\sum_{i=1}^{n_{\mathrm{MU}}}\rho_i F_t^i$, f_ζ, and f_v are functions (of time t) accounting for the activation, sarcomere length, and velocity dependencies, respectively. The total active muscle stress is the result of a superposition of the twitch force of each of the n_{MU} motor unit types present in the muscle fiber, where ρ_i indicates their corresponding fraction. The scalar factor Na is a measure of the total number of activated muscle units per reference cross-sectional area. The twitch force of a single motor unit of type i is determined by [15, 44]

$$F_t^i = G_i(T_i/I_i)\sum_{j=1}^{n_{\mathrm{IMP}}} g_{ij}(t - t_{ij}), \tag{12}$$

DOI: 10.1002/cnm

with n_{IMP} equal to the number of impulses sent to the recruited muscle fibers. The aforementioned formulation for F_t^i is based on the sum over the mechanical response of each single motor unit twitch g_{ij} multiplied by a dimensionless gain function G_i. The latter function inherits the experimentally observed nonlinear relation between single muscle fiber force and normalized stimulus rate T_i/I_i through a sigmoid relationship $S_i(T_i/I_i) = 1 - \exp\left[-2(T_i/I_i)^3\right]$. Twitch contraction time T_i and interstimulus interval I_i are experimentally determinable muscle properties. The gain function and the single twitch force response are of the form [15,44]

$$G_i(T_i/I_i) = \frac{S_i(T_i/I_i)}{T_i/I_i} = \frac{1-\exp\left[-2(T_i/I_i)^3\right]}{T_i/I_i}, \tag{13}$$

$$g_{ij}(t-t_{ij}) = \frac{(t-t_{ij})\bar{F}_i}{T_i}\exp\left[1-\frac{(t-t_{ij})}{T_i}\right], \tag{14}$$

where $\bar{F}_i$ is the twitch force of motor unit type i determined experimentally.

The expressions f_ξ and f_v in (11) are physically motivated and account for the microscopic state of the muscle. From experiments by Gordon *et al.* (1966) [53] and others, the dependence of the overlap between actin and myosin filaments on the muscle force produced by a single twitch is well understood. In the formulation described here, f_ξ is given by a Weibull distribution that depends on two characteristic constants $\lambda_{\min}$ and λ_{opt}, where $\lambda_{\min}$ denotes the lower bound for the fiber stretch at which myofilaments still overlap, and λ_{opt} refers to the fiber stretch at which maximum twitch force is reached. The asymmetric shape of the Weibull distribution properly describes the experimentally observed muscle response [15,44]. Accordingly,

$$f_\xi(\lambda_m) = \begin{cases} \frac{\lambda_m-\lambda_{min}}{\lambda_{opt}-\lambda_{min}}\exp\left[\frac{(2\lambda_{min}-\lambda_m-\lambda_{opt})(\lambda_m-\lambda_{opt})}{2(\lambda_{min}-\lambda_{opt})^2}\right] & \text{if} \lambda_m > \lambda_{min}, \\ 0 & \text{else.} \end{cases} \tag{15}$$

The hyperbolic character of the relation between the force due to concentric muscle contraction and the fiber stretch velocity $\dot{\lambda}_m$ observed in experiments by Hill (1938) [3] is included in f_v. The formulation considered here distinguishes between the muscle shortening and lengthening phase as follows [15,44]:

$$f_v(\dot{\lambda}_m) = \begin{cases} \frac{1-\dot{\lambda}_m/\dot{\lambda}_m^{min}}{1+k_c\dot{\lambda}_m/\dot{\lambda}_m^{min}} & \text{if } \dot{\lambda}_m \leq 0, \\ \frac{1+\dot{\lambda}_m/\dot{\lambda}_m^{min}}{1-k_e k_c\dot{\lambda}_m/\dot{\lambda}_m^{min}} & \text{if } \dot{\lambda}_m > 0, \end{cases} \tag{16}$$

where k_e and k_c are constants referring to the concentric and eccentric contraction and $\dot{\lambda}_{min}$ denotes the minimum stretch rate.

2.2. Implementation in the finite element package ABAQUS

In order to simulate the mechanical response of individual muscles, the model was implemented into the commercial FE package ABAQUS (Dassault Systèmes, Providence, RI, USA) [54]. It allows users to program a user subroutine called UMAT, where general material constitutive equations can be implemented. In the UMAT subroutine, the deformation gradient $\mathbf{F}$ represents an input, while the Cauchy stress tensor $\boldsymbol{\sigma}$ and the spatial tangent stiffness c^J [55,56] are output variables. The latter one is consistent with the objective Jauman–Zaremba stress rate. In particular, the Cauchy stress tensor and the spatial tangent stiffness are given by

$$\sigma_{ij} = \frac{1}{J}F_{iI}S_{IJ}F_{jJ}, \tag{17}$$

$$c^J_{ijkl} = \frac{1}{J}F_{iI}F_{jJ}\mathcal{C}_{IJKL}F_{kK}F_{lL} + \frac{1}{2}(\sigma_{ik}\delta_{jl} + \sigma_{il}\delta_{jk} + \delta_{ik}\sigma_{jl} + \delta_{il}\sigma_{jk}), \tag{18}$$

DOI: 10.1002/cnm

where S_{IJ} and $\mathcal{C}_{IJKL}$ are components of the second Piola–Kirchhoff stress tensor and material tangent modulus tensor, respectively.

The derivations of the individual terms for the second Piola–Kirchhoff stress and material tangent modulus tensor for the functional form W (1) are presented in the following, while the corresponding set of equations for the second formulation $\bar{W}$ (3) is derived in Appendix B.

The second Piola–Kirchhoff stress tensor based on (1) reads as

$$\begin{aligned}\mathbf{S} = 2\frac{\partial W}{\partial \mathbf{C}} = \frac{1}{2}\mu \Big\{ &\exp\left[\alpha\left(\tilde{I}-1\right)\right]\left(\tilde{\mathbf{L}} + w_a\mathbf{M}\right) - \exp\left[\beta\left(\tilde{J}-1\right)\right]\mathbf{C}^{-1}\tilde{\mathbf{L}}\mathbf{C}^{-1} \\ &+ \left(\tilde{J}\exp\left[\beta\left(\tilde{J}-1\right)\right] - III_C^{-\gamma}\right)\mathbf{C}^{-1}\Big\}. \end{aligned} \tag{19}$$

Taking the dependence of w_a on the right Cauchy Green tensor $\mathbf{C}$ into account, the corresponding material tangent can be given by

$$\begin{aligned}\mathcal{C} = 2\frac{\partial \mathbf{S}}{\partial \mathbf{C}} = \mu\Big\{ &\alpha\exp\left[\alpha\left(\tilde{I}-1\right)\right]\left(\tilde{\mathbf{L}} + w_a\mathbf{M}\right)\otimes\left(\tilde{\mathbf{L}} + w_a\mathbf{M}\right) \\ &+ \alpha\lambda_m^2\exp\left[\alpha\left(\tilde{I}-1\right)\right]\left(\tilde{\mathbf{L}} + \frac{1+w_a\alpha\lambda_m^2}{\alpha\lambda_m^2}\mathbf{M}\right)\otimes\frac{\partial w_a}{\partial \mathbf{C}} \\ &+ \beta\exp\left[\beta\left(\tilde{J}-1\right)\right]III_{\mathbf{C}}^2\left(\mathbf{C}^{-1}\tilde{\mathbf{L}}\mathbf{C}^{-1}\otimes\mathbf{C}^{-1}\tilde{\mathbf{L}}\mathbf{C}^{-1}\right) \\ &- \left(\beta\tilde{J}+1\right)\exp\left[\beta\left(\tilde{J}-1\right)\right]III_{\mathbf{C}}\left(\mathbf{C}^{-1}\otimes\mathbf{C}^{-1}\tilde{\mathbf{L}}\mathbf{C}^{-1} + \mathbf{C}^{-1}\tilde{\mathbf{L}}\mathbf{C}^{-1}\otimes\mathbf{C}^{-1}\right) \\ &+ \left[\left(\beta\tilde{J}+1\right)\tilde{J}\exp\left[\beta\left(\tilde{J}-1\right)\right] + \gamma III_{\mathbf{C}}^{-\gamma}\right]\mathbf{C}^{-1}\otimes\mathbf{C}^{-1} \\ &+ \left(\tilde{J}\exp\left[\beta\left(\tilde{J}-1\right)\right] - III_{\mathbf{C}}^{-\gamma}\right)\frac{\partial\mathbf{C}^{-1}}{\partial\mathbf{C}} - \exp\left[\beta\left(\tilde{J}-1\right)\right]III_{\mathbf{C}}\frac{\partial\mathbf{C}^{-1}\tilde{\mathbf{L}}\mathbf{C}^{-1}}{\partial\mathbf{C}}\Big\}, \end{aligned} \tag{20}$$

where

$$\frac{\partial w_a}{\partial \mathbf{C}} = \frac{dw_a}{d\lambda_m}\frac{\partial\lambda_m}{\partial\mathbf{C}} = \begin{cases} 0 & \text{if } P_{act} = 0, \\ \left(\frac{1}{2\alpha\lambda_m^3}\frac{dW_0(\chi^\star)}{d\lambda_m} - \frac{W_0(\chi^\star)}{\alpha\lambda_m^4} - \frac{1}{4\lambda_m^2}\frac{d^2\tilde{I}_p}{d\lambda_m^2} + \frac{1}{4\lambda_m^3}\frac{d\tilde{I}_p}{d\lambda_m}\right)\mathbf{M} & \text{otherwise.} \end{cases} \tag{21}$$

The derivatives of $\mathbf{C}^{-1}$ and $\mathbf{C}^{-1}\tilde{\mathbf{L}}\mathbf{C}^{-1}$ with respect to $\mathbf{C}$ are given in Appendix A. It should be noted that the second term on the right-hand side of (20) causes the material tangent modulus $\mathcal{C}$ to be unsymmetric.

The derivative of the Lambert-W_0 function with respect to the muscle stretch appearing in (21) is given by

$$\frac{dW_0(\chi^*)}{d\lambda_m} = \frac{1}{(1+W_0)\exp[W_0]}\frac{d\chi^*}{d\lambda_m}, \tag{22}$$

$$\begin{aligned}\frac{d\chi^*}{d\lambda_m} = \frac{2\alpha}{\mu}\exp\left[\frac{\alpha}{2}\left(2-2\tilde{I}_p + \lambda_m\frac{d\tilde{I}_p}{d\lambda_m}\right)\right]\Bigg\{ &P_{act} + \lambda_m\frac{dP_{act}}{d\lambda_m} \\ &+ \frac{\alpha}{2}P_{act}\lambda_m\left(\lambda_m\frac{d^2\tilde{I}_p}{d\lambda_m^2} - \frac{d\tilde{I}_p}{d\lambda_m}\right)\Bigg\} \\ &+ \frac{\alpha}{2}\left(1+\frac{\alpha}{2}\right)\exp\left[\frac{\alpha}{2}\lambda_m\frac{d\tilde{I}_p}{d\lambda_m}\right]\left\{\frac{d\tilde{I}_p}{d\lambda_m} + \lambda_m\frac{d^2\tilde{I}_p}{d\lambda_m^2}\right\}. \end{aligned} \tag{23}$$

The additional active muscle stress P_{act} resulting from impulses sent to the muscle is a function of λ_m. Thus, we can write

$$\frac{dP_{act}}{d\lambda_m} = Na\sum_{i=1}^{n_{\mathrm{MU}}}\rho_i F_t^i\left(f_v\frac{df_\zeta}{d\lambda_m} + f_\zeta\frac{df_v}{d\dot{\lambda}_m}\frac{\partial\dot{\lambda}_m}{\partial\lambda_m}\right), \tag{24}$$

DOI: 10.1002/cnm

where the derivatives of the functions $\{f_\zeta, f_v\}$ with respect to λ_m are given by

$$\frac{df_\zeta}{d\lambda_m} = \begin{cases} 0 & \text{if } P_{\text{act}} = 0, \\ \frac{(\lambda_{min}-\lambda_m)^2-(\lambda_{min}-\lambda_{opt})^2}{(\lambda_{min}-\lambda_{opt})^3} \exp\left[\frac{(2\lambda_{min}-\lambda_m-\lambda_{opt})(\lambda_m-\lambda_{opt})}{2(\lambda_{min}-\lambda_{opt})^2}\right] & \text{otherwise,} \end{cases} \tag{25}$$

$$\frac{df_v}{d\dot{\lambda}_m} = \begin{cases} -\frac{1+k_c}{\dot{\lambda}_m^{min}\left(1+k_c\dot{\lambda}_m/\dot{\lambda}_m^{min}\right)^2}\frac{\partial\dot{\lambda}_m}{\partial\lambda_m} & \text{if } \dot{\lambda}_m \leqslant 0, \\ \frac{1+k_e k_c}{\dot{\lambda}_m^{min}\left(1-k_e k_c\dot{\lambda}_m/\dot{\lambda}_m^{min}\right)^2}\frac{\partial\dot{\lambda}_m}{\partial\lambda_m} & \text{if } \dot{\lambda}_m > 0. \end{cases} \tag{26}$$

Finally, using the backward Euler differentiation, the time derivative of the muscle stretch $\dot{\lambda}_m$ and its derivative with respect to the muscle stretch can be approximated by

$$\dot{\lambda}_m \approx \frac{\lambda_m(t_{n+1}) - \lambda_m(t_n)}{\Delta t}, \quad \frac{\partial\dot{\lambda}_m}{\partial\lambda_m} \approx \frac{1}{\Delta t}. \tag{27}$$

3. NUMERICAL VERIFICATION

The descriptive capabilities of the proposed muscle models and the reliability of the two different constitutive formulations are evaluated in this section by direct comparison of their performance. A uniaxial tension test is used to investigate the basic mechanical response of the passive and the active components of the muscle models. Finally, a benchmark example is introduced in order to study mesh dependent effects, convergence behavior, and the model response for different modes of muscle contraction.

3.1. Passive and active uniaxial behaviors

The two different implementations were tested in a numerical example of a unit cube meshed by one element and subjected to uniaxial tension. A single fiber family is considered with its preferred direction aligned in the uniaxial loading direction. Boundary conditions were chosen such that only axial stretches are applied, and lateral surfaces of the cube are traction free. The material parameters used within this analysis are taken from Ehret *et al.* (2011) [15,45] and are given in Table I for the passive components and in Table II for the active components [‡].

Table I. Material parameters of the muscle passive material response.

μ (kPa)	α (−)	β (−)	w_0 (−)	κ/γ (kPa)
0.1599	19.69	1.190	0.7388	1000.0

Table II. Microstructural parameters of the activation functions governing w_a.

Motor unit type	Fiber type	Index i (−)	ρ_i (%)	$\bar{F}_i$ (N)	T_i (s)
Slow	I	1	5	0.025	0.020
Fast resistant	IIa	2	29	0.044	0.011
Fast fatigue	IIb	3	66	0.768	0.011

The passive material parameters from Table I were determined by least squares optimization to fit the muscle model to experimental data from [57]. These experiments quantified the purely passive and fully activated muscle response of rat *tibialis anterior* muscle. For this muscle microstructural properties are available in literature.

[‡]Note, that in comparison to [15], the parameters $\bar{F}_i$ (twitch force of motor unit type i) have been multiplied by a factor 10 in order to reproduce the data presented by [57]. Additional material parameters: $I_i = 4.0$ms $(i = 1, 2, 3)$, $Na = 52.07\text{cm}^{-2}$, $\lambda_{min} = 0.682$, $\lambda_{opt} = 1.192$, $\dot{\lambda}_m = 0.0$.

DOI: 10.1002/cnm

In uniaxial tension simulations of the active muscle presented here, the muscle is fully activated to contract to its minimal length first, before the external stretch is applied through a prescribed displacement. The simulations using the decoupled formulation show a nonphysical volume growth for rather small axial stretches, as it can be seen in Figure 1. This observation has been reported by Helfenstein *et al.* (2010) [49] for the very same numerical example but for other fiber-reinforced material models implemented according to the decoupled formulation. In their work, Helfenstein *et al.* showed that the additive split of the strain energy function might lead to undesired material responses even though the strain energy function is polyconvex. It was concluded that for deformation modes at which the fiber contribution to the total strain energy is sufficiently large, effective fiber stretch is reduced through increasing spherical deformations.

The results of the present study also demonstrate that the decoupled formulation for fiber-reinforced material models lacks to preserve volume also for active materials such as muscle (Figure 1). At the same time, it can be shown that the coupled formulation on the basis of the strain energy function W (1) adequately constrains volume changes for stretches far beyond the physiological range of soft biological tissues.

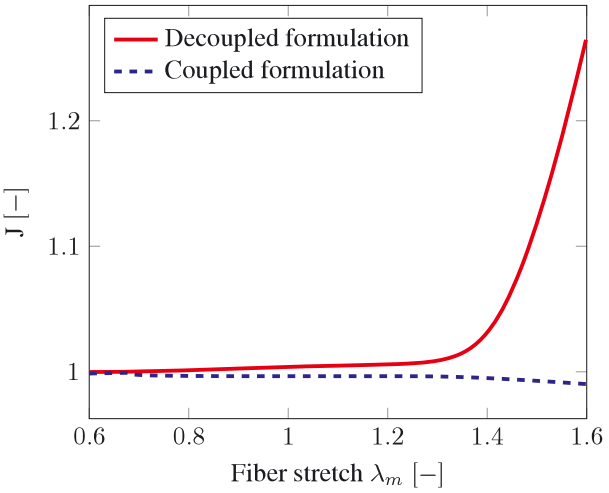

Figure 1. Element volume over fiber stretch for uniaxial stress using the fully activated muscle.

The nonphysical volumetric response was further analyzed by an eigenvalue analysis of the two different spatial tangent modulus tensors derived from W and $\bar{W}$. For each time increment in the aforementioned simulation, the six eigenstates and corresponding eigenvalues of the spatial tangents represented in the 6D space according to the Voigt notation were calculated.

According to Mehrabadi and Cowin (1990) [58] and Annin and Ostrosablin (2008) [59], these six eigenstates $\mathbf{t}^{(i)}$ possess information on principal directions of the material, and the associated eigenvalues λ_i provide a measure of corresponding stiffness. For the two implementations compared here, $\mathbf{t}^{(1)}$ points along the space diagonal of the cube, $\mathbf{t}^{(2)}$ points predominantly in the direction of the fiber, and $\mathbf{t}^{(3)}$ lies in the plane perpendicular to the fibers. Eigenstates $\mathbf{t}^{(4)}$, $\mathbf{t}^{(5)}$, and $\mathbf{t}^{(6)}$ are associated with the shearing modes and are of less interest for the case of uniaxial tension presented here (see, e.g., [58, 59]).

Figure 2 shows the evolution of the first three eigenvalues of the spatial tangent modulus tensor for: (i) the purely passive muscle and (ii) the active muscle using the decoupled formulation. In the passive case, the λ_1-curve and λ_2-curve cross. This means that the principal direction of stiffest material response changes from being along the space diagonal of the cube to the vector mainly in the direction of the fiber. This happens in the stretch range where uncontrolled volume growth begins as seen in Figure 1. To the authors knowledge, this behavior has not been presented before and provides significant information on the unphysical material response due to the decoupling of the strain energy function into a distortional and dilatational part.

DOI: 10.1002/cnm

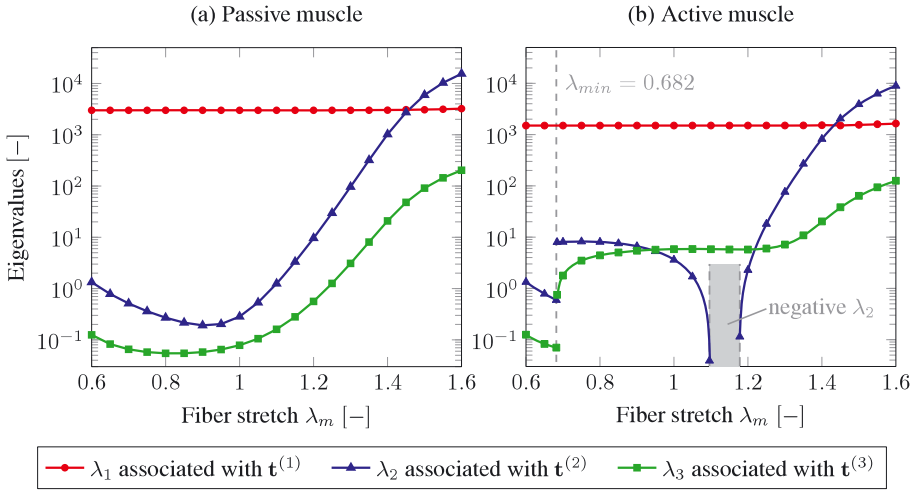

Figure 2. Evolution of the first three eigenvalues of the spatial tangent modulus tensor based on the decoupled formulation.

For the activated muscle, the similar crossing of eigenvalue curves is observed again as shown in Figure 2(b). Additionally, we also observed that for fiber stretches $\lambda_m < 0.682$, there is no contribution of the active components to the overall mechanical response of the muscle. For fiber stretches $\lambda_m \geqslant 0.682$, however, the material parameter w_a becomes nonzero, which results in a discontinuous evolution of λ_2 and λ_3. Only the eigenvalue associated with the element space diagonal (λ_1) behaves continuously and is almost constant. However, the behavior of λ_2 is most important because it becomes negative for fiber stretches λ_m between 1.1 and 1.18, while all other eigenvalues remain positive. Negative eigenvalues of the spatial tangent modulus tensor indicate nonpositive definite tangent stiffness that is unphysical for the case presented here.

Much to the contrary, the coupled formulation does not exhibit either of the problems revealed for the decoupled formulation as shown in Figure 3(a) and (b) for the passive and active muscle behaviors, respectively. For the passive muscle stretching, the eigenvalues evolve continuously, are always positive, and do not cross.

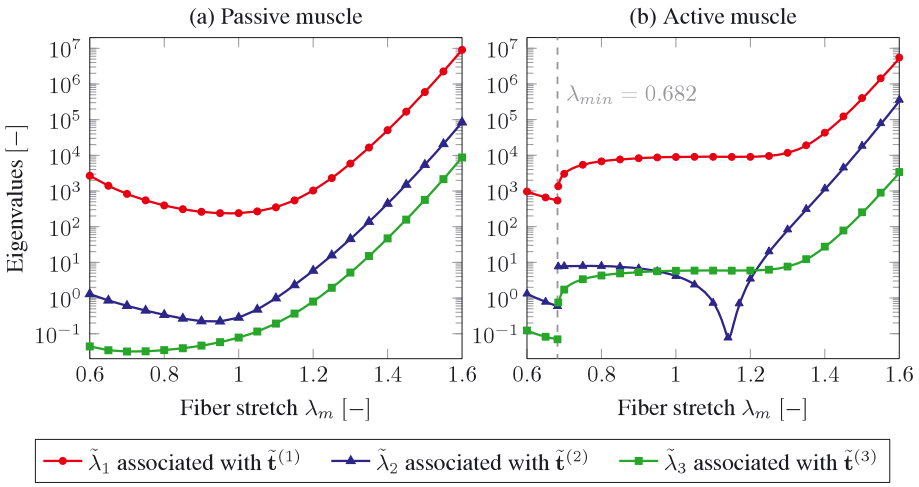

Figure 3. Evolution of the first three eigenvalues of the spatial tangent modulus tensor based on the coupled formulation.

DOI: 10.1002/cnm

The simulation of active uniaxial tension using the coupled formulation based on the strain energy function W (1) including the active material response renders only positive eigenvalues of the spatial tangent modulus tensor.

On the basis of the performance analysis of both functional forms, it can be concluded that the split of the strain energy into a volumetric and distortional part (3) leads to unphysical phenomena. Especially, the inadequately constrained volume and the negative eigenvalues present significant limitations to the applicability of this approach for the implementation of fiber-reinforced anisotropic passive and active tissue models. Hence, further verification of the muscle model implementation is carried out for the coupled functional form W (1).

3.2. Benchmark simulations

There are different modes of muscle tissue contraction depending on the activation and the kinematic boundary conditions. Generally, a distinction is made between: (i) concentric or eccentric contraction; (ii) isometric contraction; (iii) isotonic contraction; and (iv) isokinetic contraction. In the first case, the force produced upon activation is either greater or lower than the load applied to the muscle, and thus, the muscle either shortens (concentric contraction) or lengthens (eccentric contraction). Under the isometric contraction, the muscle remains at constant length, so that the force produced by the muscle balances the applied load. For the isotonic case, the contraction force of the muscle is constant and independent of changes in the muscle length. Finally, the isokinetic contraction refers to the case of constant contraction velocity.

In order to understand the model response to different contraction modes, a benchmark example is considered. The geometry is defined such that all the aforementioned modes can be simulated and combined. The setup is shown in Figure 4 where the muscle is represented by a rectangular block with a width of 100 mm, a length of 500 mm, and a thickness of 20 mm. The muscle fibers are aligned in the longitudinal direction of the block. Both ends of the muscle are tied to rigid bodies which can only move in the longitudinal direction of the block and cannot penetrate each other.

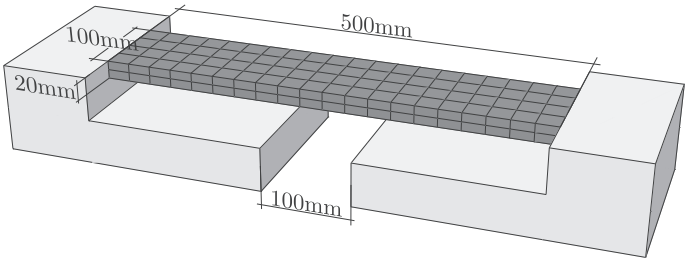

Figure 4. Geometry of benchmark model (n=2).

In the simulation, the rectangular block contracts upon activation until both rigid bodies are in contact (free contraction). Then, the contraction force increases until it reaches the maximal value corresponding to the current state of the muscle (isomeric contraction). The material parameters used for this simulation are given in Tables I and II. The muscle model was meshed by dividing the longitudinal, transverse, and height directions into $10n$, $2n$, and n segments, respectively. Therefore, the parameter n controls the level of mesh refinement. For this simulation, selective-reduced integration 8-noded hexahedral elements were used.

Figure 5 shows the evolution of the contraction force predicted in the simulation. The tetanic force is reached approximately at time t=0.08 s and remains constant for the rest of the activation time. There is no loss in tetanic force because muscle fatigue is not considered in the muscle model presented here. The gap between the two rigid bodies closes within the first 1 ms and remains closed for the remainder of the simulation time. In order to investigate the homogeneity of force in the muscle, three different levels of mesh refinement were investigated. As expected for this simple uniaxial tension case, the maximum muscle force differed by less than 1.0% when comparing meshes with $n = 1, 2, 5$. Although the inhomogeneity of the force field at the boundaries where the muscle is

DOI: 10.1002/cnm

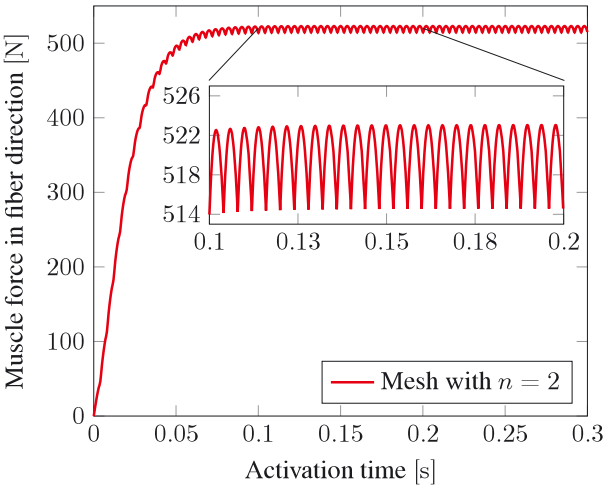

Figure 5. Tetanic muscle force in the benchmark example.

attached to the rigid bodies showed a dependency on mesh refinement, it had a minor impact on the overall response of the muscle.

The convergence behavior of the implemented material model is expressed in terms of residual force in Table III. A fixed step size of $\Delta t = 1.0 \cdot 10^{-06}$ s was defined in order to evaluate the equilibrium equations. The apparent quadratic convergence confirms the correct implementation of the material tangent for the proposed muscle model.

Table III. Convergence rate of the first four loading steps in the benchmark simulation.

	Increment #1	Increment #2	Increment #3	Increment #4
Iteration #1	$7.380 \cdot 10^{-02}$	$5.811 \cdot 10^{-03}$	$6.508 \cdot 10^{-03}$	$7.185 \cdot 10^{-03}$
Iteration #2	$1.352 \cdot 10^{-03}$	$8.512 \cdot 10^{-06}$	$1.051 \cdot 10^{-05}$	$1.261 \cdot 10^{-05}$
Iteration #3	$4.756 \cdot 10^{-07}$	$2.172 \cdot 10^{-11}$	$3.111 \cdot 10^{-11}$	$4.338 \cdot 10^{-11}$

The muscle response due to a variation in individual twitch forces $\bar{F}_i$ and interstimulus rate I_i is analyzed on the example of isometric contraction as shown in Figure 6. For this purpose, both rigid bodies are fixed, and the total muscle length of 500 mm is thus prescribed. Apart from the values of

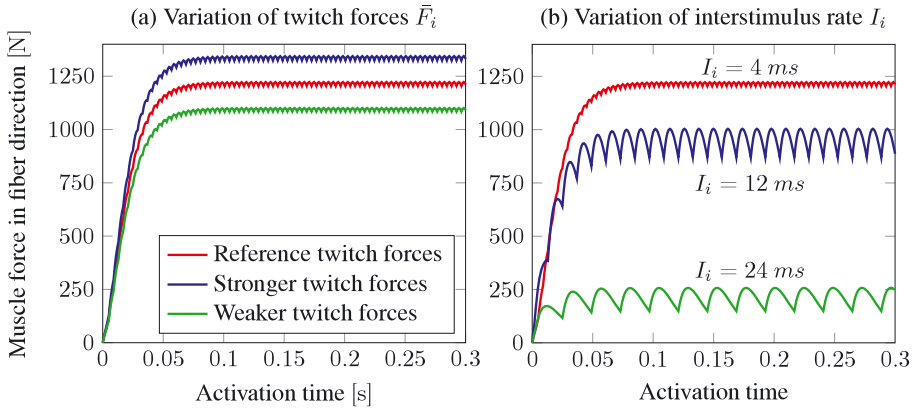

Figure 6. Parameter study on contractile properties of the masseter muscle. Influence of (a) muscle fiber twitch and (b) interstimulus rate on the active muscle force in the fiber direction.

DOI: 10.1002/cnm

F_i and I_i, material parameters are the same as in the previous simulations. The impact of the twitch force variation is investigated by varying the values of F_i (reported in Section 3.1) by $\pm 10\%$. Thus, a weaker and stronger muscle response is simulated.

It can be seen from Figure 6 that the magnitude of muscle force differs from previous simulations due to the different fiber stretches at which the muscle contracts isometrically (present case $\lambda_m = 1.0$, previous simulations $\lambda_m = 0.8$ due to isotonic contraction until rigid bodies are in contact). It can be observed that the force time history is similar to the previous example. A variation of twitch forces by $\pm$ 10% results in a corresponding variation on the tetanic forces by $\pm$ 11.0%. Furthermore, the maximum force level drops significantly for longer interstimulus times. Increasing the interstimulus rate by a factor 6 causes a drop in the maximum force by 80.0%.

4. SIMULATION OF MASSETER MUSCLE RESPONSE

The human mastication system consists of the masseter, the temporalis, the medial pterygoid, and the lateral pterygoid muscle. All of those muscles, except for the temporalis, originate from the skull and insert into the mandible. Moreover, the temporomandibular joint builds a connection point between mandible and temporal bone. Due to the shape of the joint, movements in all planes are possible, thus allowing to open and close the mouth, to move sidewise, and to grind during mastication and speech. The lateral pterygoid muscle allows to open the jaw, while the other three muscle mainly act in closing and sidewise movements of the jaw. The mastication muscle group is innervated by the mandibular branch of the trigeminal nerve.

Barbarino *et al.* (2008, 2009) [60, 61] presented an anatomically detailed FE model of the face of a 27 year old male. In their work, most facial soft tissue structures including muscles of the masticatory system were semiautomatically reconstructed from magnetic resonance images. The mechanical interactions between different tissues were represented, and the nonlinear force-deformation characteristic of soft biological materials was governed by three dimensional constitutive equations that are valid for finite elasto-viscoplastic deformations (Rubin and Bodner [62, 63]).

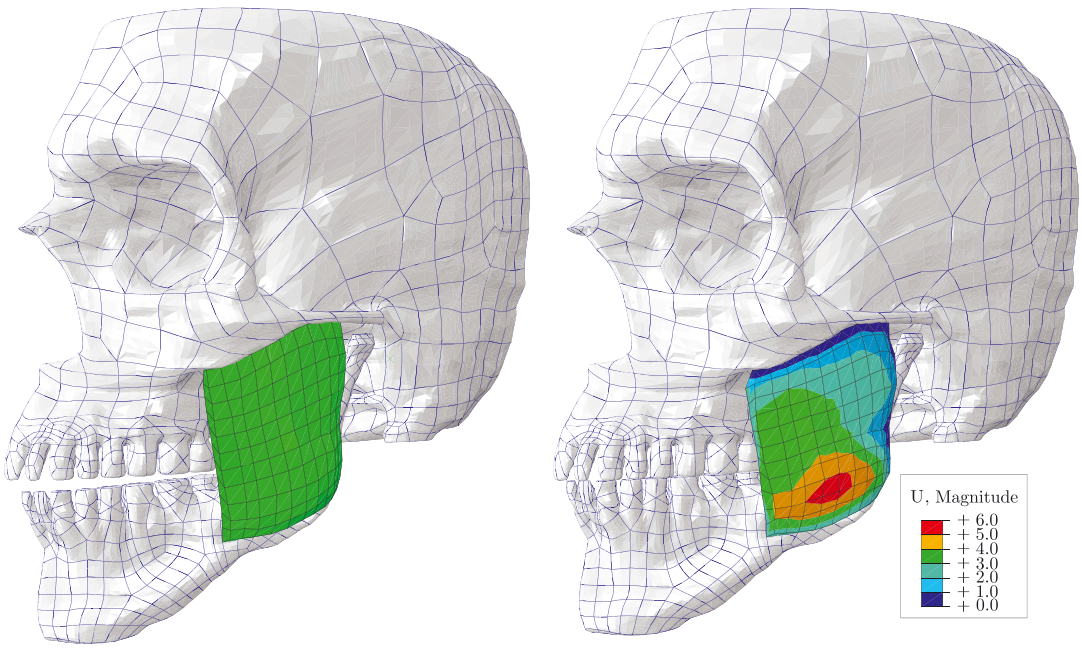

Figure 7. Anatomical reconstruction of the masseter muscle, skull, and mandible (left). The displacement magnitude of the masseter muscle at the end of the activation time (right).

The geometric representation presented here is based on the segmentation proposed in [61]. Other examples aiming at the reconstruction of such tissue structures are presented in literature

DOI: 10.1002/cnm

[20, 25, 42, 64, 65]. The masticatory system is reduced to the masseter muscle only because during mastication, the masseter muscle is dominantly responsible for the generation of bite force to be simulated in this example. The physiological resting position of the mandible (the relaxed state of the masseter muscle) is characterized by a mouth opening of 4.0 mm at the incisors [66]. A homogeneous muscle fiber alignment in the longitudinal muscle direction is assumed. The muscle insertion points are modeled by boundary conditions applied to the superior end of the muscle where it inserts into the zygomatic arch and the inferior end. Here, the muscle is connected to the inferior, posterior region of the mandible. The jaw rotates around the transverse axis, while the sagittal and vertical axes are locked. Bone structures are modeled as rigid bodies, and the masseter mesh consists of selective-reduced integration 8-node elements. A representation of the masticatory system considered in this example is shown in Figure 7.

When activating the masseter muscle, the jaw rotates around the temporomandibular joint causing the mouth to close. Once the teeth are in contact, the total muscle length is fixed, while the muscle continues to increase the contraction force until it reaches the maximum value. The bite strength of the human masticatory system has been investigated in several different ways. For example, Van Eijden (1991) [67] provided a setup allowing to determine bite force values for various bite positions and force directions. By least squares optimization, we determined material parameters on the basis of the maximal bite force of 500 N according to the range of bite forces recorded by [67].

The microstructural parameters entering the active part of the model are derived from physical properties of the human masseter. The experimental works by Eriksson and Thornell (1983) [68], Fuglevand *et al.* (1999) [69], and Yemm (1977) [70] allow to determine the distribution of muscle fiber type I (62.0%) and IIb (38.0%), as well as their respective twitch forces and contraction times. According to [68], the human masseter muscle has a negligible amount of fast twitch muscle fiber type IIa.

In Tables IV and V, the material parameters used in the numerical example are summarized, while $Na = 7.384\,\mathrm{cm}^{-2}$ in (11).

Table IV. Material parameters of the passive model determined by the least squares optimization.

μ (kPa)	α (−)	β (−)	w_0 (−)
0.165	19.96	2.02	0.736

Table V. Microstructural parameters obtained from experiments on masseter muscle fibers by Eriksson and Thornell (1983) [68], Fuglevand *et al.* (1999) [69], and Yemm (1977) [70].

Motor unit type	Fiber type	Index i (−)	ρ_i (%)	$\bar{F}_i$ (N)	T_i (s)
Slow	I	1	62.5	0.0829	0.0656
Fast fatigue	IIb	2	37.5	0.0536	0.0459

The numerical model proposed here provides not only a way to predict muscle forces but also allows to realistically estimate the 3D geometric changes in the muscle shape on the basis of the current state of contraction. As a consequence of the nearly incompressible behavior, the contraction will result in a shortening and thickening of the masseter muscle. Figure 7 shows the magnitude of displacement at the end of the contraction period. The activation will cause a rotation of the jaw until the teeth are closed. Note that the teeth opening of 4.0 mm of the incisors corresponds to a vertical displacement of about 3.31 mm in the region of the molar teeth.

The predicted bite force-time curve is plotted in Figure 8. The bite force continuously increases up to a peak force level of 500 N. The time to reach tetanic force is around 0.4 s which is in line with [20]. Moreover, the shape of the bite force curve over time closely follows data found in literature [71].

DOI: 10.1002/cnm

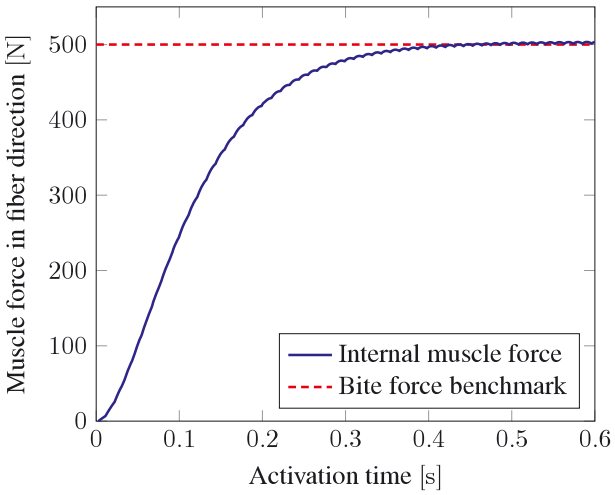

Figure 8. Masseter muscle force response during an activation period of 600 ms.

5. CONCLUSION

In the present paper, two FE implementations of a continuum constitutive model with and without the volumetric-isochoric split of the strain energy function of skeletal muscle tissue are compared. The decoupled approach is often favored in cases where volumetric and distortional material response can be expressed in terms of two individual parts in the strain energy function [72]. The passive part and the physically based active part were selected such that polyconvexity and coercivity are guaranteed. The derivation of the two corresponding Cauchy stress tensors σ and the consistent spatial tangent stiffness $\mathcal{C}^J$ are provided and implemented in the user-defined ABAQUS subroutine UMAT. A direct comparison of the two functionally different formulations revealed substantial numerical limitations of the decoupled approach. Significant volume growth takes place within a physical range of the muscle deformation and results in an unphysical representation of muscle tissue behavior. On the other hand, the coupled formulation is shown to properly predict the nearly incompressible nature of the tissue and its active response. On the basis of the eigenvalue analysis of the spatial tangent modulus tensor, it is concluded that the decoupled approach is unsuitable for anisotropic fiber-reinforced materials, both passive and active. This observation provides strong motivation to formulate the strain energy function in terms of the full right Cauchy Green tensor. In a benchmark example, the coupled model demonstrated quadratic convergence and good predictive capabilities in different loading configurations.

Finally, an anatomically based representation of the human masseter muscle was used to investigate the predictive capabilities of the model with respect to shape changes and muscle force production during the biting phase of mastication. This example shows the possibility to simulate geometrically complex structures and highly nonlinear problems including active material response.

Experimental verification of the 3D prediction of muscle shape changes during contraction is planned as a next step. Future work will also consider an anatomically based representation of muscle fiber orientation.

APPENDIX A:

Derivation for the coupled formulation

The components of the derivatives of $\mathbf{C}^{-1}$ and $\mathbf{C}^{-1}\tilde{\mathbf{L}}\mathbf{C}^{-1}$ with respect to $\mathbf{C}$ as in (20) are given by

$$\left(\frac{\partial \mathbf{C}^{-1}}{\partial \mathbf{C}}\right)_{IJKL} = -\frac{1}{2}\left(C^{-1}_{IK}C^{-1}_{JL} + C^{-1}_{IL}C^{-1}_{JK}\right), \tag{A.1}$$

DOI: 10.1002/cnm

$$\left(\frac{\partial \mathbf{C}^{-1}\tilde{\mathbf{L}}\mathbf{C}^{-1}}{\partial \mathbf{C}}\right)_{IJKL} = -\frac{1}{2}\left(C^{-1}_{IK}C^{-1}_{JM}\tilde{L}_{MN}C^{-1}_{NL} + C^{-1}_{IL}C^{-1}_{JM}\tilde{L}_{MN}C^{-1}_{NK}\right) - \frac{1}{2}\left(C^{-1}_{JK}C^{-1}_{IM}\tilde{L}_{MN}C^{-1}_{NL} + C^{-1}_{JL}C^{-1}_{IM}\tilde{L}_{MN}C^{-1}_{NK}\right). \quad (A.2)$$

APPENDIX B:

Derivation for the decoupled formulation

The equations presented here follow general concepts of continuum mechanics (as presented in, e.g., [72]). However, due to the active elements entailed in the constitutive equations presented in Section 2.1, the standard forms of the decoupled approach include additional terms. Hence, for the sake of completeness, we present the full set of equations in the following.

The second Piola–Kirchoff stress tensor $\mathbf{S}$ resulting from the strain energy function $\bar{W}$ (3) reads as

$$\mathbf{S} = 2\frac{\partial \bar{W}}{\partial \mathbf{C}} = 2\frac{\partial \bar{W}_{iso}}{\partial \bar{\mathbf{C}}} : \frac{\partial \bar{\mathbf{C}}}{\partial \mathbf{C}} + 2\frac{\partial \bar{W}_{vol}}{\partial J}\frac{\partial J}{\partial \mathbf{C}}, \quad (B.1)$$

where the derivatives of $\bar{\mathbf{C}}$ and J with respect to $\mathbf{C}$ are given by

$$\frac{\partial \bar{\mathbf{C}}}{\partial \mathbf{C}} = J^{-2/3}\left[\mathbf{II} - \frac{1}{3}\mathbf{C}\otimes\mathbf{C}^{-1}\right], \quad \frac{\partial J}{\partial \mathbf{C}} = \frac{1}{2}J\mathbf{C}^{-1}. \quad (B.2)$$

Here, the fourth-order projection tensor $\mathbf{P}$ and the fourth-order unit tensor $\mathbf{II}$ have been introduced as follows:

$$\mathbf{P} = \mathbf{II} - \frac{1}{3}\mathbf{C}^{-1}\otimes\mathbf{C}, \quad (\mathbf{II})_{ijkl} = \frac{1}{2}(\delta_{ik}\delta_{jl} + \delta_{il}\delta_{jk}). \quad (B.3)$$

Thus, (B.1) can be rewritten by

$$\mathbf{S} = \bar{\mathbf{S}}_{iso} + J\frac{\partial \bar{W}_{vol}}{\partial J}\mathbf{C}^{-1}, \quad \bar{\mathbf{S}}_{iso} = J^{-2/3}\mathbf{P}:\bar{\mathbf{S}}, \quad (B.4)$$

where

$$\bar{\mathbf{S}} = \frac{\partial \bar{W}_{iso}}{\partial \bar{\mathbf{C}}} = \frac{\mu}{2}\left\{\exp\left[\alpha\left(\bar{\tilde{I}} - 1\right)\right]\left(\tilde{\mathbf{L}} + w_a\mathbf{M}\right) - \exp\left[\beta\left(\bar{\tilde{K}} - 1\right)\right]\left(\bar{\mathbf{C}}^{-1}\tilde{\mathbf{L}}\bar{\mathbf{C}}^{-1}\right)\right\}. \quad (B.5)$$

Again, considering the dependence of w_a on the right Cauchy Green tensor $\mathbf{C}$, the material tangent corresponding to the strain energy function $\bar{W}$ (3) is

$$\begin{aligned}\mathcal{C} &= 4\frac{\partial^2 \bar{W}}{\partial \mathbf{C}\partial \mathbf{C}} = 2\frac{\partial}{\partial \mathbf{C}}\left[2\frac{\partial \bar{W}_{iso}}{\partial \bar{\mathbf{C}}} : \frac{\partial \bar{\mathbf{C}}}{\partial \mathbf{C}} + 2\frac{\partial \bar{W}_{vol}}{\partial J}\frac{\partial J}{\partial \mathbf{C}}\right] \\ &= J^{-4/3}\mathbf{P}:\bar{\mathcal{C}}:\mathbf{P}^T + 2\frac{\partial (J^{-2/3}\mathbf{P})}{\partial \bar{\mathbf{C}}}:\bar{\mathbf{S}} \\ &\quad + 4\frac{\partial^2 \bar{W}_{vol}}{\partial J\,\partial J}\frac{\partial J}{\partial \mathbf{C}}\otimes\frac{\partial J}{\partial \mathbf{C}} + 4\frac{\partial \bar{W}_{vol}}{\partial J}\frac{\partial^2 J}{\partial \mathbf{C}\partial \mathbf{C}},\end{aligned} \quad (B.6)$$

DOI: 10.1002/cnm

where

$$\begin{aligned}\bar{\mathcal{C}} = 2\frac{\partial \bar{\mathbf{S}}}{\partial \bar{\mathbf{C}}} =& \mu \left\{ \alpha \exp\left[\alpha\left(\bar{\bar{I}}-1\right)\right]\left(\tilde{\mathbf{L}}+w_a\mathbf{M}\right)\otimes\left(\tilde{\mathbf{L}}+w_a\mathbf{M}+(\mathbf{C}\colon\mathbf{M})\frac{\partial w_a}{\partial \bar{\mathbf{C}}}\right)\right.\\ &+\exp\left[\alpha\left(\bar{\bar{I}}-1\right)\right]\mathbf{M}\otimes\frac{\partial w_a}{\partial \bar{\mathbf{C}}}\\ &-\beta\exp\left[\beta\left(\bar{\bar{K}}-1\right)\right]\left(\bar{\mathbf{C}}^{-1}\tilde{\mathbf{L}}\bar{\mathbf{C}}^{-1}\right)\otimes\left(\bar{\mathbf{C}}^{-1}\tilde{\mathbf{L}}\bar{\mathbf{C}}^{-1}\right)\\ &\left.-\exp\left[\beta\left(\bar{\bar{K}}-1\right)\right]\frac{\left(\bar{\mathbf{C}}^{-1}\tilde{\mathbf{L}}\bar{\mathbf{C}}^{-1}\right)}{\partial \bar{\mathbf{C}}}\right\}.\end{aligned} \tag{B.7}$$

REFERENCES

1. Fung Y. *Biomechanics: Mechanical Properties of Living Tissues*. Springer: New York, 1993.
2. Standring S. *Gray's Anatomy: The Anatomical Basis of Clinical Practice*. Elsevier Health Sciences: UK, 2008.
3. Hill A. The heat of shortening and the dynamic constants of muscle. *Proceedings of the Royal Society of London Series B: Biological Sciences* 1938; **126**:136–195.
4. Huxley A. Muscle structure and theories of contraction. *Progress in Biophysics and Biophysical Chemistry* 1957; **7**:255–318.
5. Ettema G, Meijer K. Muscle contraction history: modified hill versus an exponential decay model. *Biological Cybernetics* 2000; **83**(6):491–500.
6. Meijer K, Grootenboer H, Koopman H, Van Der Linden B, Huijing P. A hill type model of rat medial gastrocnemius muscle that accounts for shortening history effects. *Journal of Biomechanics* 1998; **31**(6):555–563.
7. Zajac F, Muscle and tendon: properties m, scaling. *Critical Reviews in Biomedical Engineering* 1989; **17**(4):359–411.
8. Chao E, Lynch J, Vanderploeg M. Simulation and animation of musculoskeletal joint system. *Journal of Biomechanical Engineering* 1993; **115**(4 B):562–568.
9. Delp S, Loan J, Hoy M, Zajac F, Topp E, Rosen J. An interactive graphics-based model of the lower extremity to study orthopaedic surgical procedures. *IEEE Transactions on Biomedical Engineering* 1990; **37**(8):757–767.
10. Dong F, Clapworthy G, Krokos M, Yao J. An anatomy-based approach to human muscle modeling and deformation. *IEEE Transactions on Visualization and Computer Graphics* 2002; **8**(2):154–170.
11. Nussbaum M, Chaffin D, Rechtien C. Muscle lines-of-action affect predicted forces in optimization-based spine muscle modeling. *Journal of Biomechanics* 1995; **28**(4):401–409.
12. Semwal S, Hallauer J. Biomechanical modeling: implementing line-of-action algorithm for human muscles and bones using generalized cylinders. *Computers and Graphics* 1994; **18**(1):105–112.
13. Blemker SS, Delp SL. Three-dimensional representation of complex muscle architectures and geometries. *Annals of Biomedical Engineering* 2005; **33**(5):661–673.
14. Chi S-W, Hodgson J, Chen J-S, Edgerton VR, Shin DD, Roiz RA, Sinha S. Finite element modeling reveals complex strain mechanics in the aponeuroses of contracting skeletal muscle. *Journal of Biomechanics* 2010; **43**(7):1243–1250.
15. Ehret AE, Böl M, Itskov M. A continuum constitutive model for the active behaviour of skeletal muscle. *Journal of the Mechanics and Physics of Solids* 2011; **59**(3):625–636.
16. Grasa J, Ramírez A, Osta R, Muñoz M, Soteras F, Calvo B. A 3d active-passive numerical skeletal muscle model incorporating initial tissue strains validation with experimental results on rat tibialis anterior muscle. *Biomechanics and Modeling in Mechanobiology* 2011; **10**(5):779–787.
17. Hedenstierna S, Halldin P, Brolin K. Evaluation of a combination of continuum and truss finite elements in a model of passive and active muscle tissue. *Computer Methods in Biomechanics and Biomedical Engineering* 2008; **11**(6):627–639.
18. Johansson T, Meier P, Blickhan R. A finite-element model for the mechanical analysis of skeletal muscles. *Journal of Theoretical Biology* 2000; **206**(1):131–149.
19. Oomens C, Maenhout M, Van Oijen C, Drost M, Baaijens F. Finite element modelling of contracting skeletal muscle. *Philosophical Transactions of the Royal Society B: Biological Sciences* 2003; **358**(1437):1453–1460.
20. Röhrle O, Pullan A. Three-dimensional finite element modelling of muscle forces during mastication. *Journal of Biomechanics* 2007; **40**(15):3363–3372.
21. Sharifimajd B, Stålhand J. A continuum model for skeletal muscle contraction at homogeneous finite deformations. *Biomechanics and Modeling in Mechanobiology* 2012; **12**(5):965–973.
22. Böl M, Weikert R, Weichert C. A coupled electromechanical model for the excitation-dependent contraction of skeletal muscle. *Journal of the Mechanical Behavior of Biomedical Materials* 2011; **4**(7):1299–1310.
23. Röhrle O. Simulating the electro-mechanical behavior of skeletal muscles. *Computing in Science and Engineering* 2010; **12**(6):48–57.

DOI: 10.1002/cnm

24. Shorten P, O'Callaghan P, Davidson J, Soboleva T. A mathematical model of fatigue in skeletal muscle force contraction. *Journal of Muscle Research and Cell Motility* 2007; **28**(6):293–313.
25. Böl M, Stark H, Schilling N. On a phenomenological model for fatigue effects in skeletal muscles. *Journal of Theoretical Biology* 2011; **281**(1):122–132.
26. Tang C, Tsui C, Stojanovic B, Kojic M. Finite element modelling of skeletal muscles coupled with fatigue. *International Journal of Mechanical Sciences* 2007; **10**:1179–1191.
27. Dal H, Göktepe S, Kaliske M, Kuhl E. A fully implicit finite element method for bidomain models of cardiac electromechanics. *Computer Methods in Applied Mechanics and Engineering* 2013; **253**:323–336.
28. Lafortune P, Arís R, Vázquez M, Houzeaux G. Coupled electromechanical model of the heart: parallel finite element formulation. *International Journal for Numerical Methods in Biomedical Engineering* 2012; **28**(1):72–86.
29. Rossi S, Ruiz-Baier R, Pavarino L, Quarteroni A. Orthotropic active strain models for the numerical simulation of cardiac biomechanics. *International Journal for Numerical Methods in Biomedical Engineering* 2012; **28**(6-7):761–788.
30. Zöllner A, Abilez O, Böl M, Kuhl E. Stretching skeletal muscle: chronic muscle lengthening through sarcomerogenesis. *PLoS ONE* 2012; **7**(10):e45661–10p.
31. Ito D, Tanaka E, Yamamoto S. A novel constitutive model of skeletal muscle taking into account anisotropic damage. *Journal of the Mechanical Behavior of Biomedical Materials* 2010; **3**(1):85–93.
32. Böl M, Kruse R, Ehret A, Leichsenring K, Siebert T. Compressive properties of passive skeletal muscle-the impact of precise sample geometry on parameter identification in inverse finite element analysis. *Journal of Biomechanics* 2012; **45**(15):2673–2679.
33. Böl M, Leichsenring K, Weichert C, Sturmat M, Schenk P, Blickhan R, Siebert T. Three-dimensional surface geometries of the rabbit soleus muscle during contraction: input for biomechanical modelling and its validation. *Biomechanics and Modeling in Mechanobiology* 2013:1–16.
34. Siebert T, Günther M, Blickhan R. A 3d-geometric model for the deformation of a transversally loaded muscle. *Journal of Theoretical Biology* 2012; **298**:116–121.
35. Debernard L, Leclerc G, Robert L, Charleux F, Bensamoun S. *In vivo* characterization of the muscle viscoelasticity in passive and active conditions using multifrequency MR elastography. *Journal of Musculoskeletal Research* 2013; **16**(2):397–401.
36. Debernard L, Robert L, Charleux F, Bensamoun S. Characterization of muscle architecture in children and adults using magnetic resonance elastography and ultrasound techniques. *Journal of Biomechanics* 2011; **44**(3):397–401.
37. Anderson F, Pandy M. Dynamic optimization of human walking. *Journal of Biomechanical Engineering* 2001; **123**(5):381–390.
38. Praet T, Adriaens D, Cauter S, Masschaele B, Beule M, Verhegghe B. Inspiration from nature: dynamic modelling of the musculoskeletal structure of the seahorse tail. *International Journal for Numerical Methods in Biomedical Engineering* 2012; **28**(10):1028–1042.
39. Röhrle O, Davidson J, Pullan A. A physiologically based, multi-scale model of skeletal muscle structure and function. *Frontiers in Physiology* 2012; **3**:358–14p.
40. Spyrou L, Aravas N. Muscle-driven finite element simulation of human foot movements. *Computer Methods in Biomechanics and Biomedical Engineering* 2012; **15**(9):925–934.
41. Ting L, Chvatal S, Safavynia S, Lucas Mckay J. Review and perspective: neuromechanical considerations for predicting muscle activation patterns for movement. *International Journal for Numerical Methods in Biomedical Engineering* 2012; **28**(10):1003–1014.
42. Kajee Y, Pelteret J-P, Reddy B. The biomechanics of the human tongue. *International Journal for Numerical Methods in Biomedical Engineering* 2013; **29**(4):492–514.
43. Pelteret J-P, Reddy B. Computational model of soft tissues in the human upper airway. *International Journal for Numerical Methods in Biomedical Engineering* 2012; **28**(1):111–132.
44. Böl M, Reese S. Micromechanical modelling of skeletal muscles based on the finite element method. *Computer Methods in Biomechanics and Biomedical Engineering* 2008; **11**(5):489–504.
45. Ehret A. Generalised concepts for constitutive modelling of soft biological tissues. *Dissertation*, 2011.
46. Linke W, Granzier H. A spring tale: new facts on titin elasticity. *Biophysical Journal* 1998; **75**(6):2613–2614.
47. Magid A, Law D. Myofibrils bear most of the resting tension in frog skeletal muscle. *Science* 1985; **230**(4731): 1280–1282.
48. Flory P. Thermodynamic relations for high elastic materials. *Transactions of the Faraday Society* 1961; **57**:829–838.
49. Helfenstein J, Jabareen M, Mazza E, Govindjee S. On non-physical response in models for fiber-reinforced hyperelastic materials. *International Journal of Solids and Structures* 2010; **47**(16):2056–2061.
50. Hartmann S, Neff P. Polyconvexity of generalized polynomial-type hyperelastic strain energy functions for near-incompressibility. *International Journal of Solids and Structures* 2003; **40**(11):2767–2791.
51. Schröder J, Neff P. Invariant formulaiton of hyperelastic transverse isotropy based on polyconvex free energy functions. *International Journal of Solids and Structures* 2003; **40**(2):401–445.
52. Corless R, Gonnet G, Hare D, Jeffrey D, Knuth D. On the lambert W function. *Advances in Computational Mathematics* 1996; **5**(4):329–359.
53. Gordon A, Huxley A, Julian F. The variation in isometric tension with sarcomere length in vertebrate muscle fibres. *Journal of Physiology* 1966; **184**(1):170–192.
54. *ABAQUS/Standard Analysis User's Manual*. Dassault Systèmes: Providence, RI, USA, 2009.

DOI: 10.1002/cnm

55. Miehe C. Numerical computation of algorithmic (consistent) tangent moduli in large-strain computational inelasticity. *Computer Methods in Applied Mechanics and Engineering* 1996; **34**:223–240.
56. Sun W, Chaikof E, Levenston M. Numerical approximation of tangent moduli for finite element implementations of nonlinear hyperelastic material models. *Journal of Biomechanical Engineering* 2008; **130**(6):061003–7p.
57. Hawkins D, Bey M. A comprehensive approach for studying muscle-tendon mechanics. *Journal of Biomechanical Engineering* 1994; **116**(1):51–55.
58. Mehrabadi M, Cowin S. Eigentensors of linear anisotropic elastic materials. *Quarterly Journal of Mechanics and Applied Mathematics* 1990; **43**(1):15–41.
59. Annin B, Ostrosablin N. Anisotropy of elastic properties of materials. *Journal of Applied Mechanics and Technical Physics* 2008; **49**(6):998–1014.
60. Barbarino G, Jabareen M, Trzewik J, Mazza E. Physically based finite element model of the face. *Biomedical Simulation, Proceedings* 2008; **5104**:1–10.
61. Barbarino G, Jabareen M, Trzewik J, Nkengne A, Stamatas G, Mazza E. Development and validation of a three-dimensional finite element model of the face. *Journal of Biomechanical Engineering* 2009; **041006**:11 pp.
62. Rubin MB, Bodner SR. A three-dimensional nonlinear model for dissipative response of soft tissue. *International Journal of Solids and Structures* 2002; **39**(19):5081–5099.
63. Rubin MB, Bodner SR. Modeling nonlinear dissipative response of biological tissues. *International Journal of Solids and Structures* 2004; **41**(5-6):1739–1740.
64. Flynn C, Stavness I, Lloyd J, Fels S. A finite element model of the face including an orthotropic skin model under *in vivo* tension. *Computer Methods in Biomechanics and Biomedical Engineering* 2013. DOI: 10.1080/10255842.2013.820720.
65. Taylor M, Bryan R, Galloway F. Accounting for patient variability in finite element analysis of the intact and implanted hip and knee: a review. *International Journal for Numerical Methods in Biomedical Engineering* 2013; **29**(2):273–292.
66. Manns A, Miralles R, Palazzi C. Emg, bite force, and elongation of the masseter muscle under isometric voluntary contractions and variations of vertical dimension. *The Journal of Prosthetic Dentistry* 1979; **42**(6):674–682.
67. Van Eijden T. Three-dimensional analyses of human bite-force magnitude and moment. *Archives of Oral Biology* 1991; **36**(7):535–539.
68. Eriksson P-O, Thornell L-E. Histochemical and morphological muscle-fibre characteristics of the human masseter, the medial pterygoid and the temporal muscles. *Archives of Oral Biology* 1983; **28**(9):781–795.
69. Fuglevand A, Macefield V, Bigland-Ritchie B. Force-frequency and fatigue properties of motor units in muscles that control digits of the human hand. *Journal of Neurophysiology* 1999; **81**(4):1718–1729.
70. Yemm R. The orderly recruitment of motor units of the masseter and temporal muscles during voluntary isometric contraction in man. *Journal of Physiology* 1977; **265**(1):163–174.
71. Koolstra JH, van Eijden TM. A method to predict muscle control in the kinematically and mechanically indeterminate human masticatory system. *Journal of Biomechanics* 2001; **34**(9):1179–88.
72. Holzapfel GA. *Nonlinear Solid Mechanics: A Continuum Approach for Engineering*. John Wiley & Sons Ltd.: UK, 2000.